A Flexible 2D-3D Parametric Image Registration Algorithm for Cardiac MRI

L.W. Lorraine Ma and Mehran Ebrahimi[(✉)]

Faculty of Science, University of Ontario Institute of Technology,
2000 Simcoe Street North, Oshawa, ON L1H 7K4, Canada
{lok.ma,mehran.ebrahimi}@uoit.ca

Abstract. We propose a mathematical formulation aimed at parametric intensity-based registration of a deformed 3D volume to a 2D slice. The approach is flexible and can accommodate various regularization schemes, similarity measures, and optimizers. We evaluate the framework on 2D-3D registration experiments of *in vivo* cardiac magnetic resonance imaging (MRI) aimed at image-guided surgery applications that use of real-time MRI as a visualization tool. An affine transformation is used to demonstrate this parametric model. Target registration error, Jaccard and Dice indices are used to validate the algorithm and demonstrate the accuracy of the registration scheme on both simulated and clinical data.

Keywords: Image registration · Inverse problems · 2D to 3D alignment · Cardiac MRI · Optimization · Multi-level · Multi-resolution

1 Introduction

Cardiovascular disease is the leading cause of death globally, claiming more lives than cancer and chronic lower respiratory disease combined [1]. In Canada, cardiovascular disease is responsible for approximately 1 in every 3 deaths, with a quarter of those deaths resulting from myocardial infarction [2].

Ventricular arrhythmias commonly occur in patients with previous myocardial infarction due to myocardial scarring, which can disrupt electrical activity in the heart. Arrhythmias in the ventricles are potentially life-threatening because they can render the heart unable to effectively circulate blood through the body, and are associated with increased risk of sudden cardiac death [3,4].

Treatment options include catheter ablation, removing or isolating anatomic structure responsible for abnormal propagation of electrical impulses. X-ray fluoroscopy is traditionally used to guide cardiac catheterization procedures. However, because of its poor soft tissue contrast and the ionizing radiation involved, real-time magnetic resonance imaging (MRI) has been proposed as an alternative [5–7]. With superior soft tissue contrast, real-time MRI used during cardiovascular procedures would better capture anatomical features of the heart.

Real-time MRI provides live positional updates during intervention in 2D, but the tradeoff between image quality and acquisition time means that 2D real-time

MRI lacks in image quality compared to high-quality 3D MRI volumes acquired prior to intervention. Ideally, one would register the 3D prior images to 2D real-time images, combining the advantages of both to obtain high-quality images that account for small amounts of motion, such as motion due to respiration, in real time.

In this paper, we propose a mathematical framework to align high-resolution 3D MR images to noisier 2D real-time MR images. While previous work in the area focused on rigid body transformation [7–9], we extend the model to affine parametric registration and investigate ill-posedness of the registration as an inverse problem.

A general mathematical model is introduced in Sect. 2. The discretization of the model is covered in Sect. 3, followed by a Gauss-Newton optimization strategy described in Sect. 4. Computational experiments and results on both simulated and real 2D-3D data will be presented in Sect. 5. Finally, Sect. 6 is dedicated to discussion and conclusions.

2   Mathematical Model

Consider the registration problem of a 3D template image $\mathcal{T}$ to a 2D reference image $\mathcal{R}$, where $\mathcal{R}$ is a realization of $\mathcal{T}$ deformed via a transformations y and sliced at a certain location, e.g. z. The reference and template images are represented by mappings $\mathcal{R} : \Omega \subset \mathbb{R}^2 \to \mathbb{R}$ and $\mathcal{T} : \Omega \times \mathcal{Z} \subset \mathbb{R}^3 \to \mathbb{R}$ of compact support. Considering a slice location z, the goal is to find the transformation $y : \mathbb{R}^3 \to \mathbb{R}^3$ such that $\mathcal{L}_z(\mathcal{T}[y])$ is similar to $\mathcal{R}$, in which $\mathcal{T}[y]$ is the transformed template image and $\mathcal{L}_z : \mathbb{L}^2(\Omega \times \mathcal{Z}) \to \mathbb{L}^2(\Omega)$ is the slicing operator at level $z \in \mathcal{Z} \subset \mathbb{R}$, where $\mathcal{L}_z(\mathcal{T}(x^1, x^2, x^3)) := \mathcal{T}(x^1, x^2, z)$ for $(x^1, x^2, x^3) \in \mathbb{R}^3$. A formulation of the 2D-3D image registration of a template image $\mathcal{T}$ to a reference image $\mathcal{R}$ can be written as the following problem.

2D-3D Image Registration Problem: Given two images $\mathcal{R} : \Omega \subset \mathbb{R}^2 \to \mathbb{R}$ and $\mathcal{T} : \Omega \times \mathcal{Z} \subset \mathbb{R}^3 \to \mathbb{R}$ and an arbitrary given slice location $z \in \mathbb{R}$, find a transformation $y : \mathbb{R}^3 \to \mathbb{R}^3$ that minimize the objective functional

$$\mathcal{J}[y] := \mathcal{D}[\mathcal{L}_z(\mathcal{T}[y]), \mathcal{R}] + \mathcal{S}[y - y^{\text{ref}}].$$

Here, $\mathcal{D}$ is a distance that measures the dissimilarity of $\mathcal{L}_z(\mathcal{T}[y])$ and $\mathcal{R}$, and $\mathcal{S}$ is a regularization expression on the transformation y that penalizes transformations "away" from y^{ref}.

2.1   Parametric 2D-3D Registration

It is possible that y can be parametrized via parameters w. For example if y is an affine transformation, the transformation on a point $x = (x^1, x^2, x^3)$ can be expressed as

$$y(w; x) = \begin{pmatrix} w_1 & w_2 & w_3 \\ w_5 & w_6 & w_7 \\ w_9 & w_{10} & w_{11} \end{pmatrix} \begin{pmatrix} x^1 \\ x^2 \\ x^3 \end{pmatrix} + \begin{pmatrix} w_4 \\ w_8 \\ w_{12} \end{pmatrix}.$$

In general, for the parametric registration problem we equivalently aim to minimize

$$\mathcal{J}[w] := \mathcal{D}[\mathcal{L}_z(\mathcal{T}[y(w)]), \mathcal{R}] + \mathcal{S}[w - w^{\text{ref}}]. \tag{1}$$

Here we assume sum of squared distances (SSD) is the dissimilarity measure $\mathcal{D}$

$$\mathcal{D}[\mathcal{L}_z(\mathcal{T}), \mathcal{R}] = \mathcal{D}^{\text{SSD}}[\mathcal{L}_z(\mathcal{T}), \mathcal{R}] := \frac{1}{2} \int_{\Omega} (\mathcal{L}_z(\mathcal{T}(x)) - \mathcal{R}(x))^2 \, dx.$$

Furthermore, the regularization functional $\mathcal{S}$ can be defined as

$$\mathcal{S}[w - w^{\text{ref}}] := \frac{1}{2} \times (w - w^{\text{ref}})^T \mathbf{M} \, (w - w^{\text{ref}})$$

for a symmetric positive definite weight matrix $\mathbf{M}$ that acts as a regularizer (see [10, 11]).

If no regularization is imposed on w, for any pair of given images $\mathcal{R}$ and $\mathcal{T}$ the above model is ill-posed. Therefore, to yield a unique w, we require a regularizer $\mathcal{S}$ independent of the input images. The following theorem proves this claim.

Theorem 1. *Consider a given z. Any two affine transformations w^A and w^B that satisfy the following conditions yield $\mathcal{L}_z(\mathcal{T}[y(w^A; x)]) = \mathcal{L}_z(\mathcal{T}[y(w^B; x)])$:*

$$\begin{pmatrix} w_1^A \\ w_5^A \\ w_9^A \end{pmatrix} = \begin{pmatrix} w_1^B \\ w_5^B \\ w_9^B \end{pmatrix}, \begin{pmatrix} w_2^A \\ w_6^A \\ w_{10}^A \end{pmatrix} = \begin{pmatrix} w_2^B \\ w_6^B \\ w_{10}^B \end{pmatrix}, \begin{pmatrix} w_3^A - w_3^B \\ w_7^A - w_7^B \\ w_{11}^A - w_{11}^B \end{pmatrix} z + \begin{pmatrix} w_4^A - w_4^B \\ w_8^A - w_8^B \\ w_{12}^A - w_{12}^B \end{pmatrix} = \begin{pmatrix} 0 \\ 0 \\ 0 \end{pmatrix}.$$

Proof. Note that for any given z and w

$$\mathcal{L}_z[\mathcal{T}[y(w; x)]] = \mathcal{L}_z \left[T \left[\begin{pmatrix} w_1 & w_2 & w_3 \\ w_5 & w_6 & w_7 \\ w_9 & w_{10} & w_{11} \end{pmatrix} \begin{pmatrix} x^1 \\ x^2 \\ x^3 \end{pmatrix} + \begin{pmatrix} w_4 \\ w_8 \\ w_{12} \end{pmatrix} \right] \right]$$

$$= T \left[\begin{pmatrix} w_1 & w_2 & w_3 \\ w_5 & w_6 & w_7 \\ w_9 & w_{10} & w_{11} \end{pmatrix} \begin{pmatrix} x^1 \\ x^2 \\ z \end{pmatrix} + \begin{pmatrix} w_4 \\ w_8 \\ w_{12} \end{pmatrix} \right].$$

Now consider w^A and w^B that for any x^1, x^2

$$\begin{pmatrix} w_1^A & w_2^A & w_3^A \\ w_5^A & w_6^A & w_7^A \\ w_9^A & w_{10}^A & w_{11}^A \end{pmatrix} \begin{pmatrix} x^1 \\ x^2 \\ z \end{pmatrix} + \begin{pmatrix} w_4^A \\ w_8^A \\ w_{12}^A \end{pmatrix} = \begin{pmatrix} w_1^B & w_2^B & w_3^B \\ w_5^B & w_6^B & w_7^B \\ w_9^B & w_{10}^B & w_{11}^B \end{pmatrix} \begin{pmatrix} x^1 \\ x^2 \\ z \end{pmatrix} + \begin{pmatrix} w_4^B \\ w_8^B \\ w_{12}^B \end{pmatrix}.$$

Therefore for any x^1, x^2

$$\begin{pmatrix} w_1^A - w_1^B \\ w_5^A - w_1^B \\ w_9^A - w_1^B \end{pmatrix} x^1 + \begin{pmatrix} w_2^A - w_2^B \\ w_6^A - w_6^B \\ w_{10}^A - w_{10}^B \end{pmatrix} x^2 = - \left[\begin{pmatrix} w_3^A - w_3^B \\ w_7^A - w_7^B \\ w_{11}^A - w_{11}^B \end{pmatrix} z + \begin{pmatrix} w_4^A - w_4^B \\ w_8^A - w_8^B \\ w_{12}^A - w_{12}^B \end{pmatrix} \right].$$

Equating the right-hand-side and left-hand-side to zero completes the proof.

This suggests that if no regularization is imposed, the first two columns of w^A and w^B have to match. In addition, for any given third columns of w^A and w^B, a given z, and a given fourth column of w^A, we can always compute the fourth column of w^B that yields the same sliced result. This suggests that if we impose no regularization, the parameters of w have to be reduced to 9 instead of 12. In practice, since we typically have information about the reference w^{ref}, we impose regularization and keep the number of parameters as 12 in the parametric affine case.

Furthermore, regardless of how many parameters we choose for w, the registration problem may be ill-posed in theory due to the intensities of images $\mathcal{R}$ and $\mathcal{T}$. For example, if $\mathcal{R}$ is image of a disk in 2D and $\mathcal{T}$ is image of a sphere in 3D, the problem yields infinitely many solutions since infinitely many cross-sections of a sphere can yield a disk. Due to the structure of the employed input images, this does not happen in practice. That being said, we regularize the affine transformation w in all cases.

3 Discretization

Here we apply a discretize-then-optimize paradigm (see [12] and the FAIR software [11] for details) to minimize the functional in Eq. (1). Assuming that Ω, or equivalently each slice of the image, is discretized into n pixels and $\mathcal{Z}$ into l pixels, we can define discretized grids x_R and x_T respectively relating to $\mathcal{R}$ and $\mathcal{T}$ such that $x_R = [x_k^1, x_k^2]_{k=1,\ldots,n}$ and $x_T = [x_j^1, x_j^2, x_j^3]_{j=1,\ldots,n\times l}$. Expressions $\mathbf{x}_R$ and $\mathbf{x}_T$ denote discretizations of Ω and $\Omega \times \mathcal{Z}$ respectively. Throughout this paper, it is assumed that cell-centered-discretized images R, T respectively contains n and nl pixels. Furthermore, $\mathbf{y} \approx y(w; \mathbf{x}_T)$, $\mathbf{w} = w$, $R \approx \mathcal{R}(\mathbf{x}_R)$, and $T \approx \mathcal{T}(\mathbf{x}_T)$ each corresponding to a discretization. Table 1 summarizes size of the corresponding discrete variables throughout this manuscript. Discretization of the operators $\mathcal{D}$, $\mathcal{S}$ are represented by D, S (see [11]). For a given z, the discretization of the operator $\mathcal{L}_z$, denoted by L_z can be computed as

$$L_z = I_{n \times nl} := I_{n \times n} \otimes \overbrace{[0, \ldots, 0, \underbrace{1}_{\lceil l(z+\omega)/2\omega \rceil\text{-th component}}, 0, \ldots, 0]}^{1 \times l \text{ size}}$$

in which we have assumed $\mathcal{Z}$ is the interval $(-\omega, \omega)$. The discretized problem is now to minimize the functional

$$J[\mathbf{w}] := D[L_z(T(\mathbf{y}(\mathbf{w}))), R] + S(\mathbf{w} - \mathbf{w}^{\text{ref}}).$$

4 Optimization

We compute the derivative and Hessian of J denoted by dJ and H_J respectively in a Gauss-Newton approach described in Algorithm 1 [13]. For simplicity, we allow ourselves to interchangeably refer to derivatives of real-valued functions

as Jacobians as well. Hessian and Jacobian of the regularization S are denoted respectively as dS and H_S. To proceed, we represent the Jacobian of the objective function J as $dJ := \frac{\partial J}{\partial \mathbf{w}}$. Now define $L := L_z(T(\mathbf{y}(\mathbf{w})))$ and $r := L - R$. Choosing the SSD distance measure and defining $\Psi(r) := \frac{1}{2}r^T r = D[L_z(T(\mathbf{y}(\mathbf{w}))), R]$ yields $J[\mathbf{w}] = \Psi + S(\mathbf{w} - \mathbf{w}^{\text{ref}})$. Hence using the chain-rule

$$
\begin{aligned}
\frac{\partial J}{\partial \mathbf{w}} &= \left(\frac{\partial \Psi}{\partial r}\right)\left(\frac{\partial r}{\partial L}\right)\left(\frac{\partial L}{\partial T}\right)\left(\frac{\partial T}{\partial \mathbf{y}}\right)\left(\frac{\partial \mathbf{y}}{\partial \mathbf{w}}\right) + \left(\frac{\partial S}{\partial \mathbf{w}}\right) \\
&= r^T \times I_{n\times n} \times I_{n\times nl} \times dT \times d\mathbf{y} + dS \\
&= r^T \times I_{n\times n} \times I_{n\times nl} \times dT \times d\mathbf{y} + (\mathbf{w} - \mathbf{w}^{\text{ref}})^T \mathbf{M}
\end{aligned}
$$

in which $dT := \frac{\partial T}{\partial \mathbf{y}}$ represents the derivative of the interpolant and $d\mathbf{y} := \frac{\partial \mathbf{y}}{\partial \mathbf{w}}$ is the derivative of the transformation $\mathbf{y}$ with respect to $\mathbf{w}$. Derivatives $d\mathbf{y}$ and dT are both available in FAIR [11]. Finally, the Hessian of J denoted by H_J can be approximated as

$$
H_J = d^2\Psi + H_S \approx dr^T dr + H_S = dr^T dr + \mathbf{M},
$$

where

$$
dr = \left(\frac{\partial r}{\partial L}\right)\left(\frac{\partial L}{\partial T}\right)\left(\frac{\partial T}{\partial \mathbf{y}}\right)\left(\frac{\partial \mathbf{y}}{\partial \mathbf{w}}\right) = I_{n\times n} \times I_{n\times nl} \times dT \times d\mathbf{y} = I_{n\times nl} \times dT \times d\mathbf{y}.
$$

In practice, to speed up the computations, matrix-free implementation of the algorithm can be applied. We also consider different discrete representations of the image registration problem, and address the discrete problems sequentially in the so-called multi-level approach. Starting with the coarsest and thus most

Table 1. Sizes of discrete variables. n and l correspond to the number of pixels in each slice and the number of slices in the discretization, respectively.

Variable(s)	Size
R, L, r	$n \times 1$
T	$nl \times 1$
$\mathbf{x}_R$	$2n \times 1$
$\mathbf{x}_T, \mathbf{y}$	$3nl \times 1$
$\mathbf{w}, \mathbf{w}^{\text{ref}}$	12×1
S, J, Ψ	1×1
dT	$nl \times 3nl$
$d\mathbf{y}$	$3nl \times 12$
dr	$n \times 12$
dJ, dS	1×12
$H_J, H_S, \mathbf{M}$	12×12

inexpensive problem, a solution is computed, which then serves as a starting guess for the next finer discretization. This procedure has several advantages. It adds additional regularization to the registration problem (more weight is given to more important structure), it is very efficient (typically, most of the work is done on the computationally inexpensive coarse representations, and only a refinement is required on the costly finest representation), it preserves the optimization character of the problem and thus allows the use of established schemes for line searches and stopping. The use of this technique leads to optimal schemes in the sense that only a fixed number of arithmetic operations is expected for every data point and prevents the optimization problem from being trapped in a local minimum.

Algorithm 1. Minimizing $J[\mathtt{w}]$ using Gauss-Newton Approach

Initialize $[\mathtt{w}] \leftarrow [\mathtt{w}_0]$.
while not converged **do**
  Evaluate H_J and dJ at $[\mathtt{w}]$.
  Solve the descent direction from the linear equation $H_J [\delta\mathtt{w}] = -dJ^T$.
  Find a positive scalar step-size $\mathtt{s}$ using a line-search scheme.
  Update $[\mathtt{w}] \leftarrow [\mathtt{w}] + \mathtt{s}[\delta\mathtt{w}]$.
end while

---

5   Experiments and Results

5.1   Data

3D pre-procedural and 2D real-time cardiac MRI were acquired from 6 volunteers using a 1.5T MRI scanner (GE Healthcare, Waukesha, WI).

Prior 3D (cine) images: Each pre-procedural 3D volume consists of a stack of short-axis slices of the heart with a resolution of $1.37 \times 1.37 \times 8\,\mathrm{mm}^3$ and a field of view (FOV) of $350 \times 350\,\mathrm{mm}^2$. The images were acquired at end-expiration breath-hold during the end-diastolic cardiac phase with an electrocardiogram (ECG) gated GE FIESTA pulse sequence.

Real-time images: 2D real-time images were aquired at the same slice locations as in the pre-procedural scans, but under free-breathing conditions. The images were obtained with a fast spiral balanced steady state free precession sequence at a frame rate of 8 fps, an in-plane resolution of $2.2 \times 2.2\,\mathrm{mm}^2$, slice thickness $8\,\mathrm{mm}$, and a FOV of $350 \times 350\,\mathrm{mm}^2$. The images were also ECG-gated, and only end-diastole phase images were used in the following experiments.

5.2   Controlled 3D to 2D Experiments on Cardiac MRI

Controlled experiments were performed where the 2D reference image was a slice of the 3D cine volume transformed with a known affine transformation. In this example, 2D-3D registration was performed between the original 3D volume and the generated reference image where $n = 128 \times 128$, $l = 12$, $\Omega = (-175, 175) \times (-175, 175)\,\mathrm{mm}^2$, $\mathcal{Z} = (-48, 48)\,\mathrm{mm}$. Also, we assume the regularizer $\mathbf{M}$ is a diagonal 12×12 matrix with unit entries on the main diagonal except for locations 3, 7, and 11 where entries are 10^6, i.e., large. This regularizer ensures the third column of the computed $\mathbf{w}$ to be $[0, 0, 1]^T$ in practice; see Theorem 1. Linear interpolation and an Armijo line search [13] were
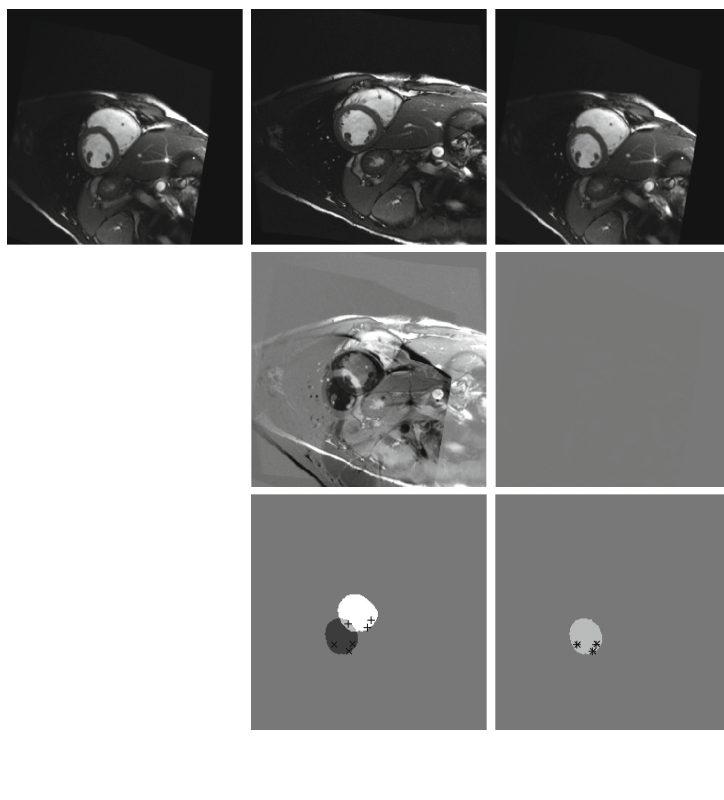

a	b	c
d	e
f	g

Fig. 1. Results of registration between a 3D image and a 2D cine image in a controlled experiment. (a) Reference image R. (b), (c) Template slice L before and after registration. (d), (e) Difference between the reference image and template slice $(L - R)$ before and after registration. (f) Segmentation masks showing left ventricle overlap before registration, with out-of-plane reference image landmarks projected onto image ($\times$) and in-plane template image landmarks ($+$). (g) Segmentation masks showing left ventricle overlap after registration, with out-of-plane reference image landmarks projected onto image ($\times$) and in-plane template image landmarks ($+$).

Table 2. Jaccard indices and Dice coefficients of left ventricle overlap before and after registration in the controlled experiment described above.

	Jaccard	Dice	TRE (mm)
Before registration	0.05	0.10	43.2 ± 4.3
After registration	1.00	1.00	1.8 ± 0.1

used in the multi-level Gauss-Newton optimization framework with a stopping criteria of 100 fixed iterations that was tuned to yield satisfactory results for our experiments.

Figure 1 shows the results of a controlled experiment where the reference image was produced by transforming a 3D cine volume with arbitrarily selected parameters $\mathbf{w} = [w_1, w_2, ..., w_{12}] = [1.2, 0.2, -0.1, 23\,\mathrm{mm}, -0.2, 1, 0.1, -41\,\mathrm{mm}, 0, 0.1, 0.9, -15\,\mathrm{mm}]$ and then slicing with L_z, where the slicing operation was applied at location $z = -4\,\mathrm{mm}$.

The Dice similarity coefficient and Jaccard index used are defined as: $\mathrm{Dice}(A, B) = \frac{2|A \cap B|}{|A| + |B|}$ and $\mathrm{Jaccard}(A, B) = \frac{|A \cap B|}{|A \cup B|}$.

The left ventricle and landmarks in the left ventricle were manually segmented in the original 3D cine image volume. The endocardium of the left ventricle was outlined for each slice in the original image volume, and the in-plane segmentations stacked to produce a 3D segmentation mask. The 3D segmentation mask was then transformed using transformation parameters obtained from the registration, i.e., $\mathbf{w}$, and then sliced at $z = -4\,\mathrm{mm}$ to obtain $L = L_z(T(\mathbf{y}(\mathbf{w})))$. Jaccard and Dice indices were then computed between the projected masks of the reference image and the slice described above. The target registration error (TRE) before registration was obtained by measuring the l^2-normed distance between the landmark locations in the initially transformed volume and in the template image. Landmark locations in the initially transformed volume (from which the 2D reference slice is taken) can be computed using the manually selected landmark locations and the initial transformation, which are known. The TRE after registration was similarly obtained from landmark locations in the template image transformed with $\mathbf{w}$, see Table 2.

5.3   3D Cine to 2D Real-Time Cardiac MRI Registration

Experiments were performed where a 2D real-time image was taken to be the reference image. 2D-3D registration was performed between a 3D cine image volume and the real-time reference image with the same parameters as in the controlled experiment, with the exception that there is no initial transformation applied on the reference image.

The real-time and cine cardiac MRI are already rather aligned initially in the z-direction so performing registration between images from different slices would be a better indicator of how well the algorithm works to move things in the z-direction. By choosing the slicing operation at location $z = -36\,\mathrm{mm}$, the initial

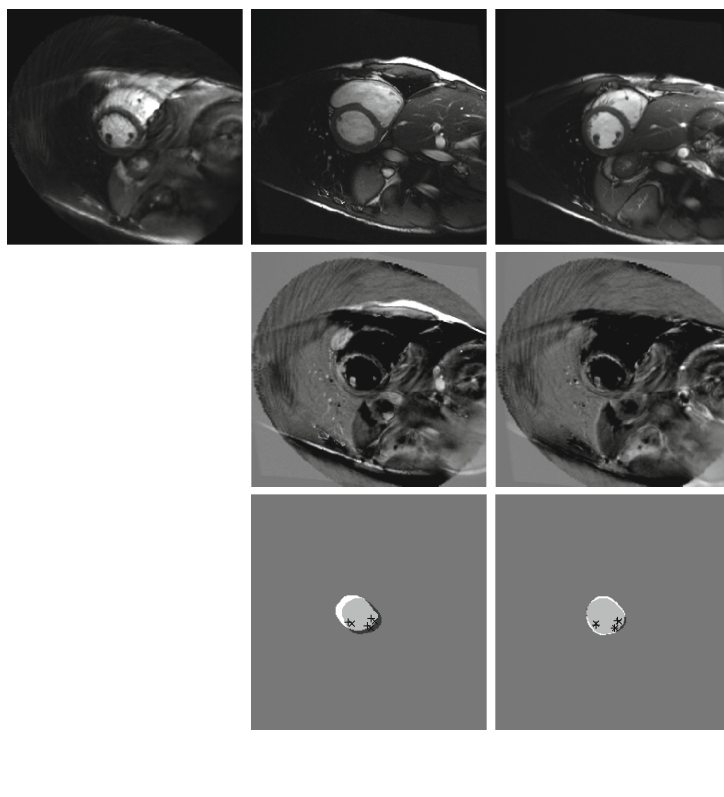|		
a	b	c
d	e	
f	g	

Fig. 2. Results of registration between a 3D cine image and a 2D real-time image on the same subject as in the controlled experiment, with an initial misalignment of approximately 32 mm in the z-direction (through the image plane). (a) Reference image R. (b), (c) Template slice L before and after registration. (d), (e) Difference between the reference image and template slice ($L - R$) before and after registration. (f) Segmentation masks showing left ventricle overlap before registration, with in-plane reference image landmarks ($\times$) and out-of-plane template image landmarks projected onto image ($+$). (g) Segmentation masks showing left ventricle overlap after registration, with in-plane reference image landmarks ($\times$) and out-of-plane template image landmarks projected onto image ($+$).

template slice was geometrically positioned approximately 32 mm away from the location of the reference image (at $z_0 = -4$ mm). To register the images, the registration algorithm must now produce a result that translates the 3D template image approximately 32 mm in the z-direction, along with appropriate alignments in the x-, y-directions. To validate registration results, the left ventricle in each of the 2D real-time images was segmented by an expert. Results including projected left ventricle overlap before and after registration are shown in Fig. 2. Jaccard and Dice indices were again computed between the projected masks of the 2D real-time image and a slice of the 3D mask transformed using parameters

Table 3. Jaccard indices and Dice coefficients of left ventricle overlap before and after registration between a 3D cine image and 2D real-time image, described above.

	Jaccard	Dice	TRE (mm)
Before registration	0.67	0.80	32.8 ± 0.3
After registration	0.87	0.93	4.5 ± 0.1

obtained from the registration. The TRE was also computed assuming that z_0, the z-coordinate location of the 2D reference image, is known. The l^2-normed distances of the landmarks in the reference image and template images before and after registration were used to compute the TREs. The results are shown in Table 3.

6   Discussion and Conclusion

In the previous section, it was demonstrated that the algorithm performs very well in controlled experiments where the reference image is a transformed and sliced version of the template image, and also where the initial misalignment due to translation alone was approximately 50 mm. The presented example was a nominal instance of several experiments performed over a range of parameters. We can conclude that between images of the same modality, the proposed multi-level parametric 2D-3D registration scheme can align images well for misalignments within reasonable limits encountered in clinical applications, such as motion due to respiration. The left ventricle overlap between the 3D cine volume and a 2D real-time image in the previous section aligned well after registration, as quantified by the Jaccard and Dice indices. The registration algorithm corrected the large z-direction translation and produced a resulting image with structural features in the heart very similar to those in the reference image as shown in Fig. 2. It is worth noting that, the regions outside the heart may not look as similar due to large motion of surrounding organs such as the lungs and diaphragm. For images of two different acquisition types – real-time and prior cine, the registration algorithm improved alignment. For multi-modality experiments where intensities differ more drastically, one can consider using other dissimilarity measures and/or optimizers [11,14] that can fit well within the context of the general proposed model.

References

1. Mozaffarian, D., et al.: Heart disease and stroke statistics - 2015 update: a report from the american heart association. Circulation **131**, e29–e322 (2015)
2. The Public Health Agency of Canada: Tracking Heart Disease and Stroke in Canada (2009)
3. Koplan, B.A., Stevenson, W.G.: Ventricular tachycardia and sudden cardiac death. Mayo. Clin. Proc. **84**, 289–297 (2009)
4. Kokolis, S., Clark, L.T., Kokolis, R., Kassotis, J.: Ventricular arrhythmias and sudden cardiac death. Prog. Cardiovasc. Dis. **48**, 426–444 (2006)
5. Lardo, A.C.: Real-time magnetic resonance imaging: diagnostic and interventional applications. Pediatr. Cardiol. **21**, 80–98 (2000)
6. Rhode, K.S., Hill, D.L.G., Edwards, P.J., et al.: Registration and tracking to integrate X-Ray and MR images in an XMR facility. IEEE Trans. Med. Imag. **22**, 1369–1378 (2003)
7. Xu, R., Wright, G.A.: Registration of real-time and prior imaging data with applications to MR guided cardiac interventions. In: Camara, O., Mansi, T., Pop, M., Rhode, K., Sermesant, M., Young, A. (eds.) STACOM 2014. LNCS, vol. 8896, pp. 265–274. Springer, Heidelberg (2015)
8. Smolíková, R., Wachowiak, M.P., Drangova, M.: Registration of fast cine cardiac MR slices to 3D preprocedural images: toward real time registration for MRI-guided procedures. In: Proceedings of the SPIE 5370, Medical Imaging 2004: Image Processing, pp. 1195–1205. SPIE, Bellingham (2004)
9. Smolíková-Wachowiak, R., Wachowiak, M.P., Fenster, A., Drangova, M.: Registration of two-dimensional cardiac images to preprocedural three-dimensional images for interventional applications. J. Magn. Reson. Im. **22**, 219–228 (2005)
10. Modersitzki, J.: Numerical Methods for Image Registration. Oxford U. Press, Oxford (2004)
11. Modersitzki, J.: FAIR: Flexible Algorithms for Image Registration. SIAM, Philadelphia (2009)
12. Haber, E., Modersitzki, J.: A multilevel method for image registration. SIAM J. Sci. Comput. **27**, 1594–1607 (2006)
13. Nocedal, J., Wright, S.J.: Numerical Optimization, 2nd edn. Springer, New York (2006)
14. Goshtasby, A.: 2-D and 3-D Image Registration. Wiley Press, New York (2005)